JACS
JOURNAL OF THE AMERICAN CHEMICAL SOCIETY
pubs.acs.org/JACS
Article

Vacancy-Induced Anionic Electrons in Single-Metal Oxides and Their Possible Applications in Ammonia Synthesis

Jingyu Yang, Jinbo Pan, Jun Deng, Yan-Fang Zhang, Yuhui Li, Yongqian Zhu, Guolin Wan, and Shixuan Du*

Cite This: J. Am. Chem. Soc. 2024, 146, 21160−21167
Read Online
ACCESS | Metrics & More | Article Recommendations | Supporting Information

ABSTRACT: Realizating of a low work function (WF) and room-temperature stability in electrides is highly desired for various applications, such as electron emitters, catalysts, and ion batteries. Herein, a criterion based on the electron localization function (ELF) and projected density of states (PDOS) in the vacancy of the oxide electride $[Ca_{24}Al_{28}O_{64}]^{4+}(4e^-)$ (C12A7) was adopted to screen out 13 electrides in single-metal oxides. By creating oxygen vacancies in nonelectride oxides, we find out 9 of them showed vacancy-induced anionic electrons. Considering the thermodynamic stability, two electrides with ordered vacancies, Nb_3O_3 and Ce_4O_3, stand out and show vacancy-induced zero-dimensional anionic electrons. Both exhibit low WFs, namely 3.1 and 2.3 eV for Nb_3O_3 and Ce_4O_3, respectively. In the case of Nb_3O_3, the ELF at oxygen vacancies decreases first and then increases during the decrease in the total number of electrons in self-consistent calculations due to Nb's multivalent state. Meanwhile, Ce_4O_3 displays promise for ammonia synthesis due to its low hydrogen diffusion barrier and low activation energy. Further calculations revealed that CeO with disordered vacancies at low concentrations also exhibits electride-like properties, suggesting its potential as a substitute for Ce_4O_3.

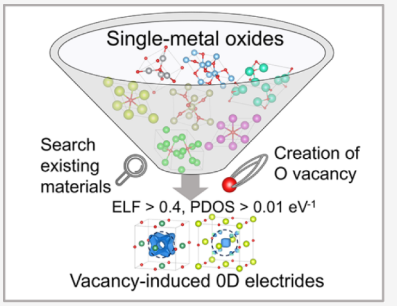

1. INTRODUCTION

Anionic electrons, as excess electrons serving as anions,[1] hold the possibility of low work function (WF) due to their loosely bound nature. Electrides, as a unique category of crystals with anionic electrons,[2] have great potential as electron providers in scientific and industrial applications, such as electron emitters, catalysts, and ion batteries.[3] The first crystalline organic electride was synthesized by Dye and coworkers in 1982.[4] Subsequently, numerous other instances of organic electrides were reported.[5−7] However, the majority of these examples suffer from poor thermal stability. The emergence of the first inorganic oxide electride, $[Ca_{24}Al_{28}O_{64}]^{4+}(4e^-)$ (C12A7),[8] altered the landscape due to its combined characteristics of room temperature stability and low WF,[9] thus leading to substantial interest and widespread applications, particularly in ammonia catalysis.[10−12] After that, various other inorganic electrides were predicted[13−15] and synthesized.[16−18]

While numerous high-throughput screenings have yielded a wealth of electrides,[19−22] the high-performance electrides, like C12A7, possessing both an exceptionally low WF (about 2.4 eV) comparable to alkali metals[23] and high stability, are still rare. C12A7, as an oxide electride formed through the introduction of vacancies, offers a viable avenue for electride creation by the generation of oxygen vacancies. The creation of oxygen vacancies is not only straightforward but also ensures commendable stability.[24,25] Introducing vacancies in such oxides holds the promise of discovering novel electrides characterized by both low WF and high stability.

Given that electrons are not precisely located in a certain position but instead exhibit a probability distribution, the assessment of anionic electrons relies on the electronic probability distribution.[26] In the earlier stage, the electrides were defined to possess a large electron localization function (ELF), e.g., >0.75,[27−29] and major contribution from anionic electron states to the electronic states around the Fermi energy[20,21,30,31] within the vacancy. However, not all reported electrides met these criteria. For example, C12A7, a well-known electride, exhibits small ELF maxima (0.45) within its oxygen vacancies.[21]

In this work, we adopted a criterion based on the ELF and projected density of states (PDOS) in the vacancies of C12A7 to look for electrides from 84 single-metal oxides in the Material Project database.[32] Despite screening existing oxides, we also created oxygen vacancies in those nonelectride oxides to discover vacancy-induced anionic electrons, which could potentially offer enhanced performance. Thirteen oxide electrides in the Materials Project and 9 oxides with vacancy-induced anionic electrons were screened out. Half of the oxide electrides described here were previously unreported. Among

Received: May 30, 2024
Revised: July 8, 2024
Accepted: July 9, 2024
Published: July 18, 2024

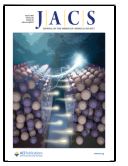

https://doi.org/10.1021/jacs.4c07362
J. Am. Chem. Soc. 2024, 146, 21160−21167

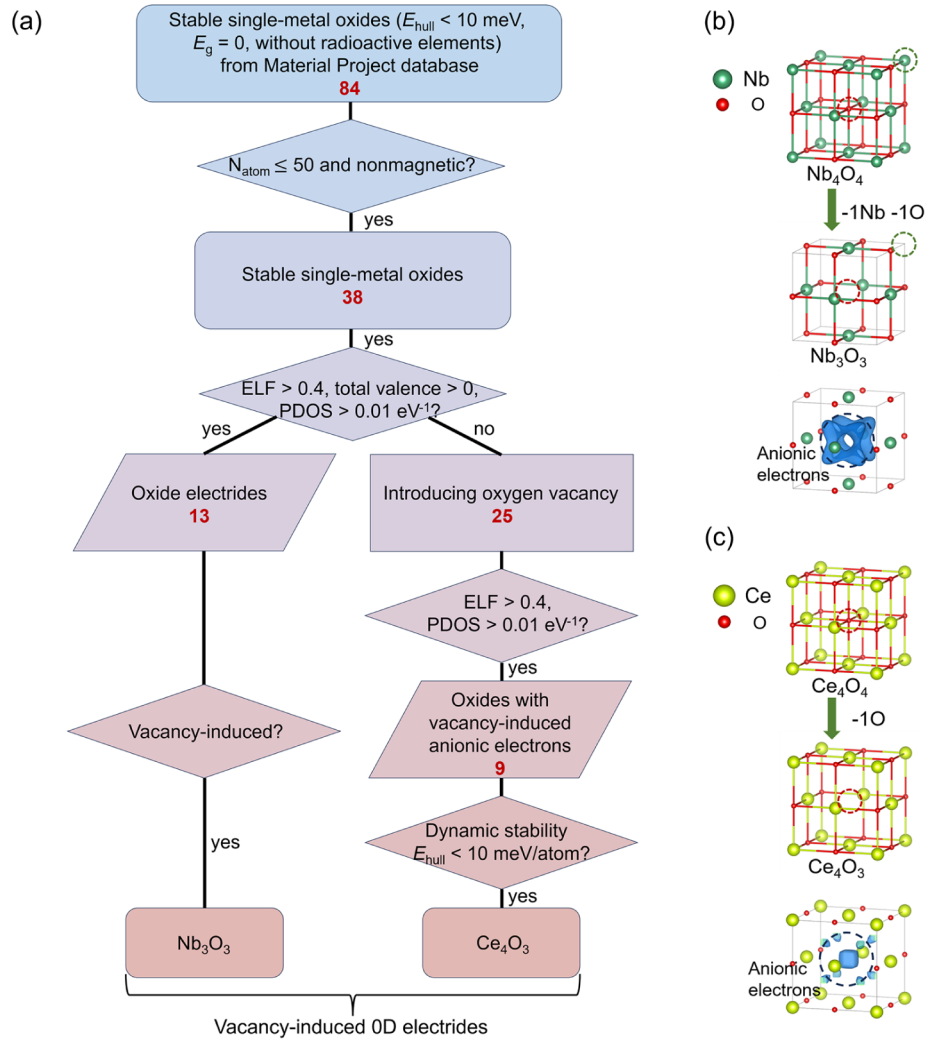

Figure 1. Screening process of vacancy-induced anionic electrons and electrides. (a) Workflow for screening vacancy-induced electrons in single-metal oxides. We chose 38 nonmagnetic materials with less than 50 atoms in a cell from 84 stable single-metal oxides in the Material Project. By considering the ELF, total valence electrons, and PDOS, 13 electrides are screened out (left). For those nonelectrides (right), we created oxygen vacancies and obtained 9 oxides with vacancy-induced anionic electrons. After considering the dynamic stability and E_{hull}, Ce_4O_3 is screened out as a stable electride. E_{hull} is the energy above the hull, and N_{atom} is the number of atoms in a unit cell. (b) Vacancy-induced 0 D electrides Nb_3O_3. (c) Vacancy-induced 0 D electrides Ce_4O_3. Vacancies are created in conventional cubic cells and marked with red (O) and green (Nb) dashed circles. Anionic electrons induced by vacancies are marked in black dashed circles with isosurface = 0.4.

them, two vacancy-induced zero-dimensional (0 D) electrides, Nb_3O_3 and Ce_4O_3, exhibit high stability and low WFs of 3.1 and 2.3 eV, respectively. Besides, Nb_3O_3's electride properties change while replacing the anionic electrons with a uniform negative background charge. Its ELF in the vacancy initially weakens and then strengthens due to its multivalent state. The vacancy electrons near the Fermi energy constantly change during the decrease of anionic electrons. Then, the application potential of low-WF electride Ce_4O_3 in ammonia synthesis was evaluated. The Ce_4O_3-supported Ru layers showed a lower N_2 dissociation barrier compared with that on pure Ru and a lower hydrogen diffusion barrier in Ce_4O_3 compared with that in C12A7. The abundant anionic vacancies and low hydrogen diffusion barrier in Ce_4O_3 indicate its high hydrogen storage capacity, which prevents excess hydrogen atoms on the Ru surface, thus, guarantees N_2 activation. Moreover, we found that CeO still exhibits anionic electron character at lower concentration of vacancies and disordered vacancies. Our research provides a new approach to the discovery of other vacancy-induced oxide electrides.

2. RESULTS AND DISCUSSION

2.1. High-Throughput Screening of Vacancy-Induced Anionic Electrons and Electrides. The high-throughput screening process is outlined in Figure 1a. Initially, we selected 84 single-metal oxides from the Material Project database.[32] These materials possess metallic properties and superior thermodynamic stability, characterized by energy above hull E_{hull} < 10 meV per atom. All of them were synthesized in the experiment and were free of radioactive elements. Among them, 38 single-metal oxides were nonmagnetic and contained less than 50 atoms ($N_{atom} \leq 50$) in a unit cell. The choice of these initial screening criteria was based on consideration of computational complexity and the potential of experimental realizations and applications.

In the following screening process, the total valence, ELF value, and average electron density around the Fermi energy

https://doi.org/10.1021/jacs.4c07362
J. Am. Chem. Soc. 2024, 146, 21160−21167

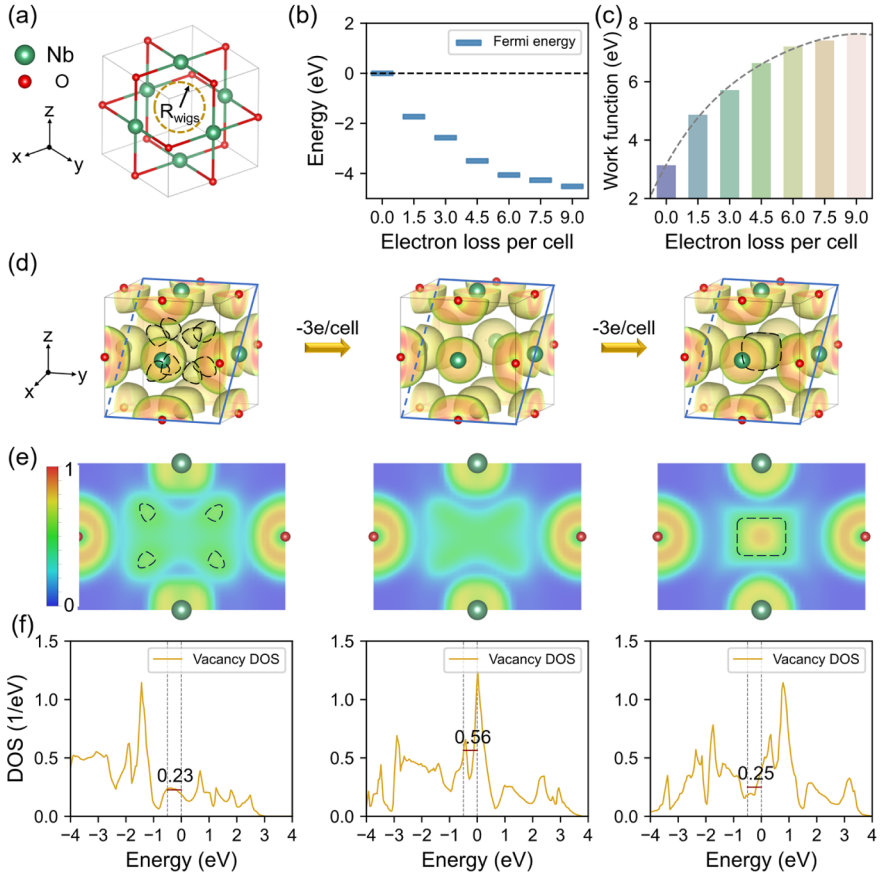

Figure 2. Properties of Nb_3O_3 during decreasing of excess electrons. The DFT+U method with U = 4 eV is used. The excess electrons are annihilated by replacing the total number of electrons in the self-consistent calculation with a negative homogeneous charge to investigate the WF and electride properties. (a) Crystal structure of Nb_3O_3. The location of vacancy-induced anionic electrons is marked with a yellow dashed circle. (b) The decline of the Fermi energy is calibrated by the states at −20.5 eV in DOS (DOS peaks, see in Section 9, Supporting Information). (c) Variation of the WF with increasing electron loss. (d) ELF of a cubic cell during electron loss for (a) Nb_3O_3:9e$^-$ (left), Nb_3O_3:6e$^-$ (middle), and Nb_3O_3:3e$^-$ (right). The isosurface is 0.46. The black dashed lines highlight the anionic electrons. (e) ELF cross-section of the (101) surface marked in Figure 2d for Nb_3O_3:9e$^-$ (left), Nb_3O_3:6e$^-$ (middle), and Nb_3O_3:3e$^-$ (right). The anionic electrons are marked with black dashed lines. (f) DOS projected on the vacancy area for Nb_3O_3:9e$^-$ (left), Nb_3O_3:6e$^-$ (middle), and Nb_3O_3:3e$^-$ (right). The black dashed lines represent the energies of −0.5 and 0 eV, while the red horizontal lines indicate the average projected density of states (PDOS) between −0.5 and 0 eV.

are considered. The DFT+U method was applied to describe oxides containing Ti, Ce, and Nb (see in Method, Section 1). First, the total valence of the compound should be positive, which means that the compound has excess electrons. All valence states are considered for elements showing multiple valence states. Second, the maximum ELF value at the vacancy site should be larger than 0.4, indicating the localized electrons within the vacancy site. Third, in the energy range of $-0.5 < E—E_f < 0$ eV, the average PDOS at the vacancy site should be larger than 0.01 eV^{-1}. The second and third criteria were established based on the properties of C12A7[21] (see the corresponding values in Figure S1). Based on the three criteria, 13 electrides were found among 38 candidates in this process (Table S1). Notably, among these 13 electrides, Nb_3O_3 ($Pm\bar{3}m$) can be regarded as Nb_4O_4 ($Fm\bar{3}m$) with ordered Nb and O vacancies.[33−37] Compared with the rock-salt phase (Nb_4O_4), the anionic electrons of Nb_3O_3 appear at the locations of its missing oxygen atoms, which confirms that the chemical environment of oxygen vacancies is prone to producing anionic electrons.

Inspired by the excellent properties of vacancy-induced electride, we introduce oxygen vacancies into the remaining 25 nonelectrides to look for stable vacancy-induced electrides with anionic electrons. Considering the vacancy concentration of Nb_3O_3, 25% or fewer oxygen vacancies were created for the 25 nonelectrides. If the number of oxygen atoms in a unit cell is less than four, a supercell is used to achieve the ≤25% oxygen vacancy concentration. Then, the calculated ELF and PDOS within their oxygen vacancies reveal that 9 of nonelectride oxides became electrides after introducing oxygen vacancies. Three of the 9 electrides with oxygen vacancies were dynamically stable, including Ce_4O_3, $Ti_{12}O_{17}$, and Ir_2O_3. The energy above the hull (E_{hull}) of Ce_4O_3 is lower than those of $Ti_{12}O_{17}$ and Ir_2O_3, indicating its high thermodynamic stability. E_{hull}, ELF, and phonon spectra of the three dynamically stable electrides are provided in Figures S4−S6.

Therefore, we finally obtained 14 electrides with high stability. The detail information including WF of the (001) surface and the E_{hull} values are summarized in Table S1. Among them, Nb_3O_3 ($Pm\bar{3}m$), TiO ($P\bar{6}2m$), Ti_3O ($P312$), three phases of Zr_3O ($R32$, $R\bar{3}c$, $P6\_32\bar{2}$), and Ce_4O_3 ($Pm\bar{3}m$) have previously been unreported as electrides. Among these metal-oxide electrides, 13 have been experimentally synthesized (Section 10 of Supporting Information), except Ce_4O_3. Since cerium oxides with different stoichiometries have been observed in experiments (Section 10 of Supporting Informa-

https://doi.org/10.1021/jacs.4c07362
J. Am. Chem. Soc. 2024, 146, 21160−21167

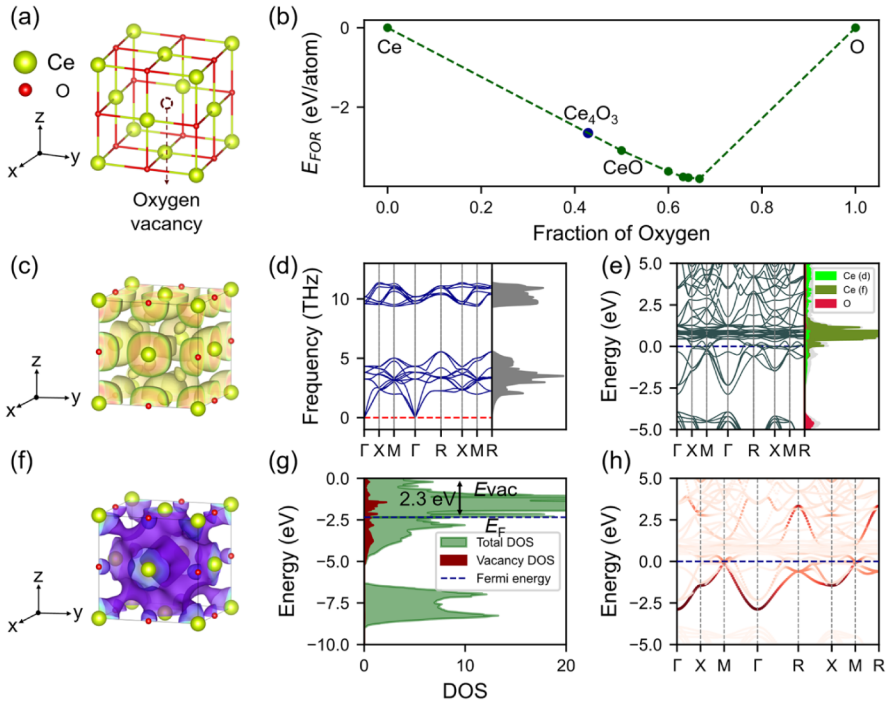

Figure 3. Stability and electronic properties of vacancy-induced electride Ce_4O_3. (a) Crystal structure of Ce_4O_3. Oxygen vacancies are marked in dashed circles. (b) Binary phase diagram of Ce and O. (c) ELF diagram, with isosurface = 0.4. (d) Phonon spectrum and phonon DOS. (e) The electronic band and projected DOS. (f) The PED of -0.5 eV < $E-E_f$ < 0 eV, the isosurface value is set to be 0.02 e bohr^{-3}. (g) Total DOS and DOS projected on oxygen vacancy. E_F is the Fermi energy. E_{vac} is the vacuum level. (h) The band structure projected on the oxygen vacancies with a fat-band character near the Fermi energy. The Fermi energy is marked in blue dashed line.

tion), we believe that Ce_4O_3 can be synthesized in the future. The two vacancy-induced electrides, Nb_3O_3 and Ce_4O_3, have anionic electrons at the position of oxygen vacancies (see in Figure 1b, c) and exhibit low WF values of 3.1 and 2.3 eV, respectively. ELF, electronic energy bands, electrostatic potentials, and partial electron density (PED) near the Fermi energies of Nb_3O_3 and Ce_4O_3 are shown in Figures S2,3.

2.2. Electron-Loss Behavior of the Transition Metal Electride Nb_3O_3. The crystal structure of Nb_3O_3 is shown in Figure 2a. As a low-WF electride, Nb_3O_3 is a transition-metal oxide with excess anionic electrons localized within oxygen vacancies. To reveal the impact of anionic electrons in Nb_3O_3, we gradually replaced them with a negative homogeneous charge to keep the system neutral (see in Section 2, Methods) and investigated their impacts on the Fermi energy, WF, and ELF. A cubic cell composed of three Nb atoms and three O atoms was used in the calculation. The decrease of Fermi energy is calibrated by the position of the states at -20.5 eV of the density of states (DOS) (Section 2, Method). The Fermi energy declines as the number of electrons in the Nb_3O_3 crystal gradually decreases in the self-consistent calculation (Figure 2b). From Figure 2c, we find that the WF experiences a rapid increase at the beginning of electron loss. Once the system loses 9 electrons, the nine excess electrons of $[Nb^{5+}{}_3O^{2-}{}_3]^{9+}(9e^-)$ are exhausted, and the change of WF tends to flatten out. This observation indicates that the WF of the electride Nb_3O_3 is closely related to its excess electrons. The ELF of Nb_3O_3 as a function of electron loss (Figure 2d,e) shows that a substantial reduction of ELF at vacancy occurs upon losing three electrons because Nb^{3+} in $[Nb_3O_3]^{3+}$ is also a common valence state of Nb. Therefore, Nb_3O_3 manifests the nonelectride characteristics of $[Nb^{3+}{}_3O^{2-}{}_3]^{3+}$ upon losing three electrons. Remarkably, the vacancy ELF value increases again as the cell loses six electrons, indicating the electride characteristics of $[Nb^{5+}{}_3O^{2-}{}_3]^{9+}(3e^-)$. Next, the DOS within a sphere of the Wigner–Seitz radius at the oxygen vacancy is calculated (Figure 2f). As the electrons of Nb_3O_3 are losing, the anionic electrons in the vacancy near the Fermi energy, indicated by the vacancy DOS between the two black dashed lines, are constantly changed, and in abundance ($\gg$0.01 eV^{-1}). In conclusion, Nb_3O_3 is a significant low-WF electride with abundant localized anionic electrons in its oxygen vacancy.

2.3. Stability and Electronic Properties of Low-WF Electride Ce_4O_3. Similar to Nb_3O_3, Ce_4O_3 is also a 0 D vacancy-induced electride (Figure 3a). Due to the high contribution of f-state electrons near the Fermi energy (Figure 3e), the DFT + U method[38,39] with U = 3 eV was used (see in Section 1, Method). The phonon spectrum (Figure 3b) shows no imaginary frequencies, while the formation energy resides on the convex hull of the Ce–O binary phase diagram (Figure 3d), indicating the high dynamic and thermodynamic stability of Ce_4O_3. The total energy of atomic Ce and CeO is slightly higher (14 meV per formula) than that of Ce_4O_3, suggesting the thermodynamic stability of Ce_4O_3. The high diffusion barrier and higher final state energy compared with the initial state also suggest the high stability of Ce_4O_3 (CeO with 25% O vacancies). $Ti_{12}O_{17}$ also exhibits a high diffusion barrier and a higher final state energy than that of the initial state (Figures S20,21). The diagram of ELF and PED near the Fermi energy (Figures 3c,f) and their (101) cross-section (Figure S7) show that Ce_4O_3 has a large ELF and PED values near the Fermi energy in its oxygen vacancy. So, Ce_4O_3 has abundant localized anionic electrons within its oxygen vacancies and can be identified as vacancy-induced electride. Moreover, the

https://doi.org/10.1021/jacs.4c07362
J. Am. Chem. Soc. 2024, 146, 21160–21167

calculated PDOS and projected band of anionic electrons show that most of the anionic electron states (the red states in Figure 3g, h) in Ce_4O_3 are distributed near the Fermi energy. We also find that Ce_4O_3's WF (2.3 eV) is lower than that of C12A7 (2.4 eV). As a vacancy-induced 0 D electride, Ce_4O_3 has extremely low WF and high stability, rendering it suitable for applications as an electron provider in e-gun and catalysis.

2.4. Potential of Ce_4O_3 in Ammonia Synthesis. Catalysts utilized in ammonia synthesis[40] have received extensive attention due to their pivotal role in both industry and agriculture.[41] Due to the high bond energy of N−N and the large energy gap between the lowest unoccupied molecular orbital (LUMO) and highest occupied molecular orbital (HOMO), N_2 activation is a bottleneck in ammonia synthesis.[42] Benefiting from the low WF and interstitial spaces or vacancy sites, electrides always serve as electron providers of catalysts to reduce the activation energy of N_2 dissociation and as hydrogen storage hosts to avoid surface hydrogen poisoning in ammonia synthesis.[3] C12A7-supported Ru-related catalysts have been successfully used in ammonia synthesis.[42,43] Considering the low WF and abundant vacancy sites due to the high oxygen vacancy concentration of Ce_4O_3, we evaluated the potential application of Ce_4O_3 in ammonia synthesis. The relative energy levels in Figure 4b reveal the potential of the electron transfer from Ce_4O_3 to Ru. Figure 4a outlines the schematic mechanism involving electrides in ammonia synthesis, in which the electrons of low-WF electride transfer to the transition metal (Ru), promoting the dissociation of N_2 adsorbed on Ru. Meanwhile, dissociated H_2 can diffuse into the vacancies of Ce_4O_3, avoiding hydrogen poisoning on the catalyst surface.

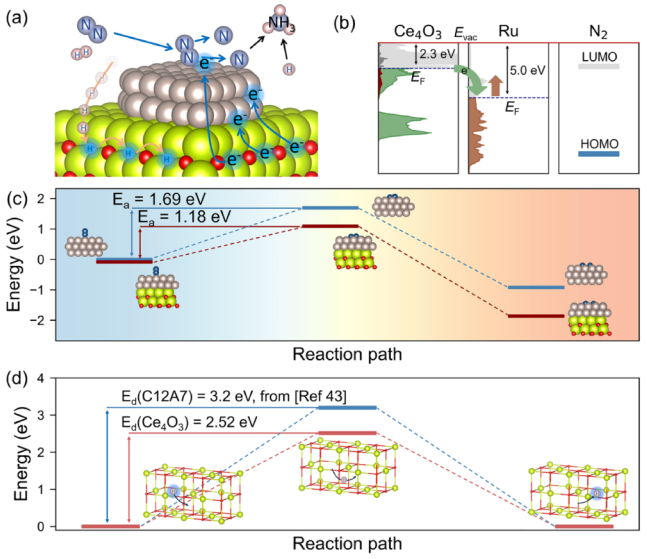

Figure 4. Ce_4O_3 and Ru participate in ammonia synthesis. (a) Schematic diagram of the mechanism by which electride Ce_4O_3 participates in ammonia synthesis. Vacancy-induced electride provides electrons to promote nitrogen activation on Ru and stores hydrogen atoms by its vacancies. (b) The mechanism of activation of N_2 molecules by electride and transition metal. The low-WF Ce_4O_3 transfers electrons to Ru, elevating the Fermi energy of Ru and making nitrogen activation more likely to occur. (c) N_2 dissociation processes on pure Ru (blue line) and Ru/Ce_4O_3 (red line). E_a is the activation energy. (d) Energy barrier E_d of H diffusion in Ce_4O_3 compared with that in C12A7[43] and a schematic diagram of the H diffusion path. The reaction path is defined as the trajectory of H as it diffuses from one oxygen vacancy to another. A 10 × 10 × 10 Å supercell of Ce_4O_3 was used for the H diffusion calculation.

In order to validate the potential of Ce_4O_3 in ammonia synthesis, first-principles calculations are performed on N_2 dissociation and hydrogen diffusion, which were two key processes in ammonia synthesis. A model with 3 layers of 5 × 5 Ru(0001) and a 20 Å vacuum layer is used for pure Ru catalyst, while a model including bilayer Ru(0001) on 4 layers of Ce-terminated Ce_4O_3(111) and 20 Å vacuum layer is used for Ru-loaded Ce_4O_3. By considering different adsorption sites and stacking configurations (Figures S8−S14), we obtained the configuration of Ce_4O_3-supported Ru with the lowest total energy (Figure S13). Using this configuration, the adsorption energy of N_2 on Ce_4O_3-supported Ru was −1.09 eV, lower than that on pure Ru (−0.83 eV). The WF of the Ce-terminated (111) surface of Ce_4O_3 was around 3.2 eV (see in Figure S15). Then, the N_2 activation energies on pure Ru and Ce_4O_3-supported Ru were calculated by using the climbing image-nudged elastic band (CI-NEB) method[44] (see in Section 1, Method). Notably, the activation energy (E_a) of N_2 on Ce_4O_3-supported Ru is 1.18 eV, which is lower than that on pure Ru (1.69 eV) (Figure 4c). Moreover, the reaction product on Ru-loaded Ce_4O_3 was more stable than that of Ru. Bader analysis[45−48] was applied to evaluate the charge transfer of N_2/Ru, Ru/Ce_4O_3, and N_2/Ru/Ce_4O_3. The results show that (Table S3) when bilayer Ru atoms are placed on Ce_4O_3, 7.34 electrons are transferred to bilayer Ru. Upon N_2 adsorption, 0.18 electrons are transferred from Ru to N_2 for N_2/Ru. The transferred electrons increased to 0.22 for N_2/Ru/Ce_4O_3. The calculation results substantiate the mechanism depicted in Figure 4a that electrides can help N_2 obtain more electrons, thereby promoting the N_2 activation process.

In addition to N_2 activation energy, hydrogen storage capacity is of great significance in ammonia synthesis.[3] In the conventional Ru catalysts, hydrogen adsorption is preferred over nitrogen adsorption on Ru, which retards the NH_3 synthesis rate. The hydrogen storage capacity of electrides prevents excess hydrogen atoms on the Ru surface, thus guaranteeing the N_2 activation. So, the hydrogen diffusion process of Ce_4O_3 was also evaluated. The H atom can diffuse from one vacancy to another through the gap between the Ce and the O atoms in Ce_4O_3 (Figures 4d). The diffusion barrier was then obtained in a 10 × 10 × 10 Å supercell of Ce_4O_3 containing 56 atoms by the CI-NEB method. The diffusion barrier E_a for H atoms within Ce_4O_3 is 2.52 eV, which was lower than that in C12A7 (3.2 eV) (Figure 4d).[43] The lower diffusion barrier indicates that the diffusion of hydrogen atoms in Ce_4O_3 is easier than in C12A7, which is beneficial for hydrogen atom storage and for avoiding surface hydrogen poison. In conclusion, Ce_4O_3 achieves high stability, low activation energy, and a low hydrogen diffusion barrier simultaneously, indicating its application potential in ammonia synthesis.

Considering the potential difficulty of single-crystal fabrication with either high concentration or ordering in experiments, CeO with a low concentration and disordered vacancies was also considered. As shown in Figure S16, the WF of CeO is 2.4 eV, slightly higher than that of Ce_4O_3 (2.3 eV). So, CeO without vacancies and those with low-concentration vacancies also have low WFs. As depicted in Figure S17a−i, with low oxygen-vacancy concentrations, CeO still fulfills the criterion of anionic electrons. Additionally, the vacancy electrons are even more localized within CeO with a low

https://doi.org/10.1021/jacs.4c07362
J. Am. Chem. Soc. 2024, 146, 21160−21167

vacancy concentration (manifested by an increase in ELF). Figure S17j–l present a supercell of CeO with three randomly positioned oxygen vacancies, demonstrating that even random vacancies retain anionic electrons. Consequently, the arrangement of vacancies is not a prerequisite for the presence of vacancy-induced anionic electrons. This insight signifies that disordered oxygen-deficient CeO, experimentally more feasible to produce, can serve as a substitute for the electride Ce_4O_3.

Finally, we take a holistic view of the experimental realization and possible applications of the electrides presented in Table S1. Due to the difficulty of directly observing anionic electrons, the discovery of new electrides in experiments often relies on measuring other properties, such as electron transport properties and WF, combined with theoretical calculations.[16] Though all of the metal-oxide electrides listed in Table S1 were synthesized experimentally except Ce_4O_3, 6 of them were previously unreported electrides due to different criteria. Alkali metal-oxide electrides, including Cs_3O, Cs_7O, Rb_9O_2, and Rb_6O, have low WFs, which enable electrons to escape from the solid under low-energy excitations and create photoemissive surfaces suitable for light detection with high quantum efficiency and high threshold wavelengths.[49] However, their applications in catalysis are limited due to their overly reactive chemical properties. Titanium oxides, including Ti_2O, Ti_6O, Ti_3O ($P312$), Ti_3O ($P\bar{3}1c$), TiO, and Zr_3O ($P6\_32\bar{2}$), have also been synthesized experimentally but have not yet been widely utilized in electron emitters or catalysis due to their high WFs. Zr_3O ($R\bar{3}c$), Zr_3O ($R32$), and Nb_3O_3 are previously unreported electrides with low WFs (3.1–3.4 eV), which may have broader chemical applications as electron donors or reductants. Although not synthesized, Ce_4O_3 simultaneously possesses an ultralow WF (2.3 eV), a large number of oxygen vacancies (25%), a lower hydrogen diffusion barrier (2.5 eV) than C12A7 and high thermodynamic stability (E_{hull} = 0). These properties meet the demands of various physical applications, such as electron emitters, light detection, and chemical applications, such as ammonia synthesis and hydrogen storage.

3. CONCLUSION AND OUTLOOK

The criteria for electride evaluation adopted from C12A7 (ELF > 0.4, average PDOS within oxygen vacancy > 0.01 eV^{-1}) enable us to screen out several electrides in single-metal oxides and those with O vacancies. Introducing vacancies to produce electride offers a promising way to look for anionic electrons from nonelectride metal oxides. A high concentration (up to 25%) of oxygen vacancies in vacancy-induced electrides provides more electron anions and more hydrogen storage spaces compared with other electrides, which is important in ammonia synthesis. The transition metal oxide electride Nb_3O_3 exhibits the special behavior of vacancy electrons. Its vacancy ELF changes during the loss of excess electrons, with a decrease followed by an increase due to its multivalent state. Ce_4O_3, a low-WF electride, has potential applications in ammonia synthesis with a low hydrogen diffusion barrier and N_2 activation energy. Moreover, CeO exhibits anionic electrons and metallic properties at low oxygen vacancy concentration and with disordered oxygen vacancies. Thus, an O-deficient CeO is a potential alternative to low-WF electride Ce_4O_3. Since oxides tend to form stable structures with O vacancies and vacancy-induced anionic electrons, more vacancy-induced electrides are worth exploring in other oxides.

4. METHODS

4.1. DFT Calculation. Lattice constants, geometric relaxations, PED, ELF, DOS, phonon spectrum, energy above the hull, energy band structure, electrostatic potential, and absorption energy of vacancy-induced anionic electrons and electrides were calculated using DFT within projector-augmented wave (PAW) potentials and the PBE exchange-correlation functional[50] as implemented in the Vienna *ab initio* simulation package (VASP) code.[51,52] A plane-wave basis set with an energy cutoff of 500–600 eV was used, and the vdW-dispersion energy-correction term was considered during the absorption energy calculations by the DFT-D3 method,[53,54] which was derived by Grimme et al. Monkhorst–Pack Brillouin zone sampling grids[55] with a resolution of 0.02 × 2π $Å^{-1}$ were applied. The structures studied were fully relaxed until the force converged to 0.01 eV $Å^{-1}$. Due to the different U values for different materials, we did not use the DFT+U method during the screening process. DFT+U[38,39] is known to be necessary to describe the reduction of Ti(IV), Nb(V), and Ce(IV). In the following process, U = 4 and U = 2.5 eV were used for Nb and Ti, respectively, as in previous reports.[56,57] A U value of 3 eV was used for Ce, as suggested for cerium oxides, including nonstoichiometric CeO_{2-x} phases.[58] The results show similar features with those obtained using the HSE06 functional[59] (Figure S19). The PDOS and fat band diagrams of anionic electrons in Ce_4O_3 and Nb_3O_3 in Figures 2 and 3 were calculated within a sphere of the Wigner–Seitz radius at the oxygen vacancy. The minimum energy pathway and energy barrier for the elementary steps of N_2 activation, H diffusion, and O diffusion were calculated using the climbing image-nudged elastic band (CI-NEB)[44] by VASP and VTST package.[60−62]

Calculations of the PDOS at the vacancy site during the screening process were done by projecting the DOS on a sphere at the vacancy site with a radius of the covalent radius of the oxygen atom for the oxides.

4.2. Calibration of Fermi Energy and Electron Loss Calculations. Compared with nonelectrides, electrides exhibit lower WFs and localized anionic electrons due to the presence of excess electrons. If the number of anionic electrons in the system decreases, the properties of the electrides will change, for example, decrease of ELF at anionic sites and increase of WF (the decline of Fermi energy).[22] The variation of the electride properties of Nb_3O_3 was obtained by a computational trick, namely, by gradually reducing the total number of electrons in self-consistent calculations. The reduction of the total number of electrons amounts to the reduction of the highest-energy electrons, which are the anionic electrons. They were replaced by a homogeneous negative background so that the crystal remained neutral. The DOS was also calculated to calibrate the decline of Fermi energy. As shown in Figure S18, the state with a DOS peak at −20.5 eV was selected as the reference. Since the energy is far away from the Fermi energy, it can be regarded as not affected by the electron loss. According to the energy difference between the peak and Fermi energy, we can derive the extent of the Fermi energy decline.

■ ASSOCIATED CONTENT

Supporting Information

The Supporting Information is available free of charge at https://pubs.acs.org/doi/10.1021/jacs.4c07362.

https://doi.org/10.1021/jacs.4c07362
J. Am. Chem. Soc. 2024, 146, 21160−21167

Electrides, oxide vacancies, and catalysis in this article (PDF)

AUTHOR INFORMATION

Corresponding Author

Shixuan Du − *Beijing National Laboratory for Condensed Matter Physics and Institute of Physics, Chinese Academy of Sciences, Beijing 100190, PR China; University of Chinese Academy of Sciences, Chinese Academy of Sciences, Beijing 100190, PR China; Songshan Lake Materials Laboratory, Dongguan 523808, PR China;* orcid.org/0000-0001-9323-1307; Email: sxdu@iphy.ac.cn

Authors

Jingyu Yang − *Beijing National Laboratory for Condensed Matter Physics and Institute of Physics, Chinese Academy of Sciences, Beijing 100190, PR China; University of Chinese Academy of Sciences, Chinese Academy of Sciences, Beijing 100190, PR China;* orcid.org/0000-0003-2299-3966

Jinbo Pan − *Beijing National Laboratory for Condensed Matter Physics and Institute of Physics, Chinese Academy of Sciences, Beijing 100190, PR China; University of Chinese Academy of Sciences, Chinese Academy of Sciences, Beijing 100190, PR China; Songshan Lake Materials Laboratory, Dongguan 523808, PR China*

Jun Deng − *Beijing National Laboratory for Condensed Matter Physics and Institute of Physics, Chinese Academy of Sciences, Beijing 100190, PR China;* orcid.org/0000-0003-2420-8079

Yan-Fang Zhang − *University of Chinese Academy of Sciences, Chinese Academy of Sciences, Beijing 100190, PR China*

Yuhui Li − *Beijing National Laboratory for Condensed Matter Physics and Institute of Physics, Chinese Academy of Sciences, Beijing 100190, PR China; University of Chinese Academy of Sciences, Chinese Academy of Sciences, Beijing 100190, PR China*

Yongqian Zhu − *Beijing National Laboratory for Condensed Matter Physics and Institute of Physics, Chinese Academy of Sciences, Beijing 100190, PR China; University of Chinese Academy of Sciences, Chinese Academy of Sciences, Beijing 100190, PR China*

Guolin Wan − *Beijing National Laboratory for Condensed Matter Physics and Institute of Physics, Chinese Academy of Sciences, Beijing 100190, PR China; University of Chinese Academy of Sciences, Chinese Academy of Sciences, Beijing 100190, PR China*

Complete contact information is available at: https://pubs.acs.org/10.1021/jacs.4c07362

Notes

The authors declare no competing financial interest.

ACKNOWLEDGMENTS

We thank K.X. Chen for discussing the concept of vacancy-induced anionic electrons. We also thank Lei Tao, Juxia Yi, and Peixuan Li for the helpful discussion about the calculation method. This work was supported by funds from the National Natural Science Foundation of China (61888102, 52272172, 11974045), the Major Program of the National Natural Science Foundation of China (92163206), the National Key Research and Development Program of China (2022YFA1204100, 2021YFA1201501) and the Fundamental Research Funds for the Central Universities. Computational resources were provided by the Tier3 Data Center in Ulanqab and National Supercomputing Center in Tianjin.

REFERENCES

(1) Dye, J. L. Electrons as anions. *Science* **2003**, *301* (5633), 607−608.
(2) Liu, C.; Nikolaev, S. A.; Ren, W.; Burton, L. A. Electrides: A review. *J. Mater. Chem. C* **2020**, *8* (31), 10551−10567.
(3) Hosono, H.; Kitano, M. Advances in Materials and Applications of Inorganic Electrides. *Chem. Rev.* **2021**, *121* (5), 3121−3185.
(4) Le, L. D.; Issa, D.; Vaneck, B.; Dye, J. L. Preparation of alkalide and electride films by direct vapor deposition. *J. Phys. Chem.* **1982**, *86* (1), 7−9.
(5) Ward, D. L.; Huang, R. H.; Dye, J. L. Structures of alkalides and electrides. I. Structure of potassium cryptand[2.2.2] electride. *Acta Crystallogr., Sect. C: Cryst. Struct. Commun.* **1988**, *44* (8), 1374−1376.
(6) Wagner, M. J.; Huang, R. H.; Eglin, J. L.; Dye, J. L. An electride with a large six-electron ring. *Nature* **1994**, *368* (6473), 726−729.
(7) Huang, R. H.; Wagner, M. J.; Gilbert, D. J.; Reidy-Cedergren, K. A.; Ward, D. L.; Faber, M. K.; Dye, J. L. Structure and Properties of Li^+ (Cryptand [2.1.1])e^-, an Electride with a 1D "Spin-Ladder-like" Cavity-Channel Geometry. *J. Am. Chem. Soc.* **1997**, *119* (16), 3765−3772.
(8) Matsuishi, S.; Toda, Y.; Miyakawa, M.; Hayashi, K.; Kamiya, T.; Hirano, M.; Tanaka, I.; Hosono, H. High-Density Electron Anions in a Nanoporous Single Crystal: $[Ca_{24}Al_{28}O_{64}]^{4+}(e^-)_4$. *Science* **2003**, *301* (5633), 626−629.
(9) Toda, Y.; Yanagi, H.; Ikenaga, E.; Kim, J. J.; Kobata, M.; Ueda, S.; Kamiya, T.; Hirano, M.; Kobayashi, K.; Hosono, H. Work function of a room-temperature, stable electride $[Ca_{24}Al_{28}O_{64}]^{4+}(e^-)_4$. *Adv. Mater.* **2007**, *19* (21), 3564−3569.
(10) Miyakawa, M.; Kim, S. W.; Hirano, M.; Kohama, Y.; Kawaji, H.; Atake, T.; Ikegami, H.; Kono, K.; Hosono, H. Superconductivity in an Inorganic Electride $12CaO{\bullet}7Al_2O_3$: e^-. *J. Am. Chem. Soc.* **2007**, *129* (23), 7270−7271.
(11) Lalan, V.; Ganesanpotti, S. The smallest anions, induced porosity and graphene interfaces in C12A7: e^- electrides: A paradigm shift in electromagnetic absorbers and shielding materials. *J. Mater. Chem. C* **2022**, *10* (3), 969−982.
(12) Hayashi, F.; Toda, Y.; Kanie, Y.; Kitano, M.; Inoue, Y.; Yokoyama, T.; Hara, M.; Hosono, H. Ammonia decomposition by ruthenium nanoparticles loaded on inorganic electride C12A7: e^-. *Chem. Sci.* **2013**, *4* (8), 3124−3130.
(13) Li, K.; Blatov, V. A.; Wang, J. Discovery of Electrides in Electron-Rich Non-Electride Materials via Energy Modification of Interstitial Electrons. *Adv. Funct. Mater.* **2022**, *32* (17), 2112198.
(14) Bae, S.; Espinosa-García, W.; Kang, Y.-G.; Egawa, N.; Lee, J.; Kuwahata, K.; Khazaei, M.; Ohno, K.; Kim, Y. -H.; Han, M. J.; et al. MXene Phase with C3 Structure Unit: A Family of 2D Electrides. *Adv. Funct. Mater.* **2021**, *31* (24), 2100009.
(15) Zhu, Q.; Frolov, T.; Choudhary, K. Computational discovery of inorganic electrides from an automated screening. *Matter* **2019**, *1* (5), 1293−1303.
(16) Lee, K.; Kim, S. W.; Toda, Y.; Matsuishi, S.; Hosono, H. Dicalcium nitride as a two-dimensional electride with an anionic electron layer. *Nature* **2013**, *494* (7437), 336−340.
(17) Lu, Y. F.; Li, J.; Tada, T.; Toda, Y.; Ueda, S.; Yokoyama, T.; Kitano, M.; Hosono, H. Water Durable Electride Y_5Si_3: Electronic Structure and Catalytic Activity for Ammonia Synthesis. *J. Am. Chem. Soc.* **2016**, *138* (12), 3970−3973.
(18) Zhang, Y. Q.; Xiao, Z. W.; Kamiya, T.; Hosono, H. Electron Confinement in Channel Spaces for One-Dimensional Electride. *J. Phys. Chem. Lett.* **2015**, *6* (24), 4966−4971.
(19) Tada, T.; Takemoto, S.; Matsuishi, S.; Hosono, H. High-throughput ab initio screening for two-dimensional electride materials. *Inorg. Chem.* **2014**, *53* (19), 10347−10358.

(20) Wan, B.; Lu, Y.; Xiao, Z.; Muraba, Y.; Kim, J.; Huang, D.; Wu, L.; Gou, H.; Zhang, J.; Gao, F.; et al. Identifying quasi-2D and 1D electrides in yttrium and scandium chlorides via geometrical identification. *Npj Comput. Mater.* **2018**, *4* (1), 77.
(21) Wang, J.; Zhu, Q.; Wang, Z.; Hosono, H. Ternary inorganic electrides with mixed bonding. *Phys. Rev. B* **2019**, *99* (6), 064104.
(22) Zhang, X.; Meng, W.; Liu, Y.; Dai, X.; Liu, G.; Kou, L. Magnetic Electrides: High-Throughput Material Screening, Intriguing Properties, and Applications. *J. Am. Chem. Soc.* **2023**, *145* (9), 5523−5535.
(23) Kiejna, A.; Wojciechowski, K. F. Work function of metals: Relation between theory and experiment. *Prog. Surf. Sci.* **1981**, *11* (4), 293−338.
(24) Zhu, H. J.; Wang, C.; He, Y.; Pu, Y.; Li, P.; He, L.; Huang, X.; Tang, W.; Tang, H. Oxygen vacancies engineering in electrocatalysts nitrogen reduction reaction. *Front. Chem.* **2022**, *10*, 1039738.
(25) Pacchioni, G. Oxygen vacancy: The invisible agent on oxide surfaces. *ChemPhysChem* **2003**, *4* (10), 1041−1047.
(26) Dale, S. G.; Johnson, E. R. Theoretical Descriptors of Electrides. *J. Phys. Chem. A* **2018**, *122* (49), 9371−9391.
(27) Savin, A.; Nesper, R.; Wengert, S.; Fässler, T. F. ELF: The electron localization function. *Angew. Chem., Int. Ed.* **1997**, *36* (17), 1808−1832.
(28) Silvi, B.; Savin, A. Classification of chemical bonds based on topological analysis of electron localization functions. *Nature* **1994**, *371* (6499), 683−686.
(29) Zhang, Y. W.; Wang, H.; Wang, Y. C.; Zhang, L. J.; Ma, Y. M. Computer-Assisted Inverse Design of Inorganic Electrides. *Phys. Rev. X* **2017**, *7* (1), 011017.
(30) Dale, S. G.; Otero-de-la-Roza, A.; Johnson, E. R. Density-functional description of electrides. *Phys. Chem. Chem. Phys.* **2014**, *16* (28), 14584−14593.
(31) Zhao, S.; Kan, E.; Li, Z. Electride: From computational characterization to theoretical design. *Wiley Interdiscip. Rev.-Comput. Mol. Sci.* **2016**, *6* (4), 430−440.
(32) Jain, A.; Ong, S. P.; Hautier, G.; Chen, W.; Richards, W. D.; Dacek, S.; Cholia, S.; Gunter, D.; Skinner, D.; Ceder, G.; et al. Commentary: The Materials Project: A materials genome approach to accelerating materials innovation. *APL Mater.* **2013**, *1* (1), 011002.
(33) Burdett, J. K.; Mitchell, J. F. Pair potentials and the ordered defect structure of niobium monoxide. *Inorg. Chem.* **1993**, *32* (23), 5004−5006.
(34) Efimenko, A. K.; Hollmann, N.; Hoefer, K.; Weinen, J.; Takegami, D.; Wolff, K. K.; Altendorf, S. G.; Hu, Z.; Rata, A. D.; Komarek, A. C.; et al. Electronic signature of the vacancy ordering in NbO (Nb_3O_3). *Phys. Rev. B* **2017**, *96* (19), 195112.
(35) Kubaschewski, O.; Hopkins, B. E. Oxidation mechanisms of niobium, tantalum, molybdenum and tungsten. *J. Less-Common Met.* **1960**, *2* (2−4), 172−180.
(36) Gusev, A. I. Anisotropy of elastic properties of cubic Nb_3O_3 niobium monoxide. *Solid State Commun.* **2023**, *372*, 115310.
(37) Gusev, A. I. Niobium monoxide superstructures. *JETP Lett.* **2020**, *111* (3), 176−182.
(38) Mosey, N. J.; Liao, P.; Carter, E. A. Rotationally invariant ab initio evaluation of Coulomb and exchange parameters for DFT+U calculations. *J. Chem. Phys.* **2008**, *129* (1), 014103.
(39) Mosey, N. J.; Carter, E. A. Ab initio evaluation of Coulomb and exchange parameters for DFT+ U calculations. *Phys. Rev. B* **2007**, *76* (15), 155123.
(40) Wang, S.; Ichihara, F.; Pang, H.; Chen, H.; Ye, J. Nitrogen fixation reaction derived from nanostructured catalytic materials. *Adv. Funct. Mater.* **2018**, *28* (50), 1803309.
(41) Erisman, J. W.; Sutton, M. A.; Galloway, J.; Klimont, Z.; Winiwarter, W. How a century of ammonia synthesis changed the world. *Nat. Geosci.* **2008**, *1* (10), 636−639.
(42) Kitano, M.; Kanbara, S.; Inoue, Y.; Kuganathan, N.; Sushko, P. V.; Yokoyama, T.; Hara, M.; Hosono, H. Electride support boosts nitrogen dissociation over ruthenium catalyst and shifts the bottleneck in ammonia synthesis. *Nat. Commun.* **2015**, *6* (1), 6731.
(43) Kammert, J.; Moon, J.; Cheng, Y.; Daemen, L.; Irle, S.; Fung, V.; Liu, J.; Page, K.; Ma, X.; Phaneuf, V.; et al. Nature of reactive hydrogen for ammonia synthesis over a Ru/C12A7 electride catalyst. *J. Am. Chem. Soc.* **2020**, *142* (16), 7655−7667.
(44) Henkelman, G.; Uberuaga, B. P.; Jónsson, H. A climbing image nudged elastic band method for finding saddle points and minimum energy paths. *J. Chem. Phys.* **2000**, *113* (22), 9901−9904.
(45) Henkelman, G.; Arnaldsson, A.; Jonsson, H. A fast and robust algorithm for Bader decomposition of charge density. *Comput. Mater. Sci.* **2006**, *36* (3), 354−360.
(46) Yu, M.; Trinkle, D. R. Accurate and efficient algorithm for Bader charge integration. *J. Chem. Phys.* **2011**, *134* (6), 064111.
(47) Sanville, E.; Kenny, S. D.; Smith, R.; Henkelman, G. Improved grid-based algorithm for Bader charge allocation. *J. Comput. Chem.* **2007**, *28* (5), 899−908.
(48) Tang, W.; Sanville, E.; Henkelman, G. A grid-based Bader analysis algorithm without lattice bias. *J. Phys.-Condes. Matter* **2009**, *21* (8), 084204.
(49) Band, A.; Albu-Yaron, A.; Livneh, T.; Cohen, H.; Feldman, Y.; Shimon, L.; Popovitz-Biro, R.; Lyahovitskaya, V.; Tenne, R. Characterization of oxides of cesium. *J. Phys. Chem. B* **2004**, *108* (33), 12360−12367.
(50) Paier, J.; Hirschl, R.; Marsman, M.; Kresse, G. The Perdew-Burke-Ernzerhof exchange-correlation functional applied to the G2−1 test set using a plane-wave basis set. *J. Chem. Phys.* **2005**, *122* (23), 234102.
(51) Kresse, G.; Furthmuller, J. Efficiency of ab-initio total energy calculations for metals and semiconductors using a plane-wave basis set. *Comput. Mater. Sci.* **1996**, *6* (1), 15−50.
(52) Kresse, G.; Furthmuller, J. Efficient iterative schemes for ab initio total-energy calculations using a plane-wave basis set. *Phys. Rev. B* **1996**, *54* (16), 11169−11186.
(53) Grimme, S.; Antony, J.; Ehrlich, S.; Krieg, H. A consistent and accurate ab initio parametrization of density functional dispersion correction (DFT-D) for the 94 elements H-Pu. *J. Chem. Phys.* **2010**, *132* (15), 154104.
(54) Car, R.; Parrinello, M. Unified approach for molecular-dynamics and density-functional theory. *Phys. Rev. Lett.* **1985**, *55* (22), 2471−2474.
(55) Monkhorst, H. J.; Pack, J. D. Special points for Brillouin-zone integrations. *Phys. Rev. B* **1976**, *13* (12), 5188−5192.
(56) Migas, D. B.; Filonov, A. B.; Borisenko, V. E.; Skorodumova, N. V. Effect of polaron formation on electronic, charge and magnetic properties of $Nb_{12}O_{29}$. *J. Alloys Compd.* **2020**, *821*, 153527.
(57) Hu, Z. P.; Metiu, H. Choice of U for DFT+U Calculations for Titanium Oxides. *J. Phys. Chem. C* **2011**, *115* (13), 5841−5845.
(58) Loschen, C.; Carrasco, J.; Neyman, K. M.; Illas, F. First-principles LDA plus U and GGA plus U study of cerium oxides: Dependence on the effective U parameter. *Phys. Rev. B* **2007**, *75* (3), 035115.
(59) Heyd, J.; Scuseria, G. E.; Ernzerhof, M. Hybrid functionals based on a screened Coulomb potential. *J. Chem. Phys.* **2003**, *118* (18), 8207−8215.
(60) Sheppard, D.; Xiao, P.; Chemelewski, W.; Johnson, D. D.; Henkelman, G. A generalized solid-state nudged elastic band method. *J. Chem. Phys.* **2012**, *136* (7), 074103.
(61) Sheppard, D.; Henkelman, G. Paths to which the nudged elastic band converges. *J. Comput. Chem.* **2011**, *32* (8), 1769−1771.
(62) Sheppard, D.; Terrell, R.; Henkelman, G. Optimization methods for finding minimum energy paths. *J. Chem. Phys.* **2008**, *128* (13), 134106.

https://doi.org/10.1021/jacs.4c07362
J. Am. Chem. Soc. 2024, 146, 21160−21167